The Report Committee for Ye Kuang
Certifies that this is the approved version of the following report:

A Continuum Modeling Approach for the Deposition of Enamel

APPROVED BY
SUPERVISING COMMITTEE:

Supervisor:

Chad M. Landis

Mark E. Mear

A Continuum Modeling Approach for the Deposition of Enamel

by

Ye Kuang, B.E.

Report

Presented to the Faculty of the Graduate School of

The University of Texas at Austin

in Partial Fulfillment

of the Requirements

for the Degree of

Master of Science in Engineering

The University of Texas at Austin

December, 2015

Acknowledgements

I would like to express my sincerest gratitude to my advisor Prof. Chad Landis. His knowledge and kindness guided me through the research and writing of this report.

Thanks to my family for all the support.

Abstract

A Continuum Modeling Approach for the Deposition of Enamel

Ye Kuang, M.S.E

The University of Texas at Austin, 2015

Supervisor: Chad M. Landis

In this report continuum methods to analyze organogenesis on curved surfaces is devised. This initial study will investigate a basic system. Dental enamel is the example system used to study the simulation of organogenesis as well as pattern formation. It is observed that dental enamel is created by a number of ameloblast cells migrating generally outward from the dental enamel junction (DEJ). These cells also rearrange locally within the surface that they reside. In this report, the simulations are based on the postulate that the cell motion arises from changes in the local strain environment as the cells migrate. As opposed to a passive movement driven by external driving forces or energy gradients, this theory hypothesizes that motion can arise internally due to the migration of the individual cell influenced by the local cell density and the velocity of the cell relative to its contacting neighbors. To model this kinematically driven approach we first develop a set of continuum equations to describe the velocity of the cells. This consists of two components, one the governs the in-plane rearrangements of the cells based on local strain cues, and a second that governs the

velocity of the cells normal to the DEJ, which depends upon if the cells are actively secreting or not. This second feature requires the knowledge of the location of the boundary between secretory and non-secretory cells, which we is called the commencement front. On the secretory side of the commencement front the normal velocity of the cells is a specified quantity, while on the non-secretory side the normal velocity is zero. In order to track the evolution of the commencement front a phase-field description is utilized that treats this boundary as a diffuse instead of a sharp interface. The numerical method that is used to solve the equations is described, and some initial preliminary results for simple surface geometries are presented.

Table of Contents

List of Tables

List of Figures

Chapter 1: Introduction

In this report I will devise continuum methods to analyze organogenesis on curved surfaces. This initial study will investigate a basic system. Dental enamel is the example system for us to study the simulation of organogenesis as well as pattern formation. Dental enamel is comprised of a brittle and weak natural mineral (hydroxyapatite), with only 1-3% protein or other material present [1-5], and the ameloblast cells that deposit the hydroxyapatite neither die nor proliferate significantly during migration. That is, their number remains the same until amelogenesis ends [3]. These conditions make this system both easier to simulate and easier to observe and conduct experiments.

It is observed that dental enamel is created by a number of ameloblasts migrating generally outward from the dental enamel junction (DEJ). The DEJ can be thought of as a curved surface in space where the ameloblasts reside prior to the beginning of their migration journey, see Figure 1. The ameloblasts migrate out-of-plane to give the enamel its thickness and in-plane to give the enamel a microstructure. For the in-plane movements there can be reorganizations of the local ameloblast cell neighbors causing a wavy, fracture-resistant microstructure to form giving the resultant enamel its toughness. As these local rearrangements occur the ameloblasts are continuously depositing mineral and smoothly advancing away from the DEJ surface in approximately the normal direction.

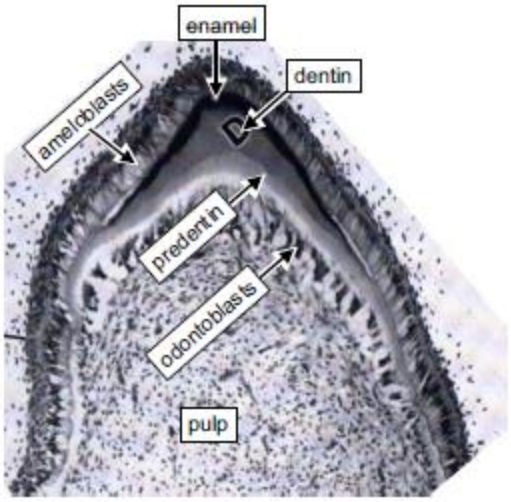

Figure 1: The tooth system, from References [4, 6].

To model the organogenesis processes, there are at least three different mechanisms to consider as primary drivers. One is that the structure is formed by chemical signals as postulated by Turing [7], which requires modeling of reaction-diffusion phenomenon [8]. Most current models of organogenesis regard cells just as a continuum, e.g., with proliferation, differentiation, and migration calculated using tensor growth functions [19-22]. A second is that gradients in strain energy (either stress in a volume or surface energy) might be the driver of the cell movements [9-17]. However, in this report, the simulations are based on a third mechanism that Cox develops [4, 18], which proposes that the motion arises from changes in the local strain environment as the cells migrate. As opposed to a passive movement driven by external driving forces or energy gradients, this theory hypothesizes that motion can arise internally due to the migration of the individual cell influenced by the local cell density and the velocity of the cell relative to its contacting neighbors.

To model this kinematically driven approach we first develop a set of continuum equations to describe the velocity of the cells. This consists of two components, one that governs the in-plane rearrangements of the cells based on local strain cues, and a second that governs the velocity of the cells normal to the DEJ, which depends upon if the cells are actively secreting or not. This second feature requires the knowledge of the location of the boundary between secretory and non-secretory cells, which we will call the commencement front. On the secretory side of the commencement front the normal velocity of the cells is a specified quantity, while on the non-secretory side the normal velocity is zero. In order to track the evolution of the commencement front we will utilize a phase-field description that treats this boundary as a diffuse instead of a sharp interface. In the following sections we introduce the governing equations for this model description, the numerical method that is used to solve the equations, as well as some initial preliminary results for simple surface geometries.

Chapter 2: Surface Parameterization

As described in the Introduction, the DEJ is a surface in three-dimensional space and all of the equations to be solved for the model will be solved on this surface. Hence, we begin with a geometric description of the surface that will be utilized within the model. The equation of a surface in a three-dimensional space can be written as

$$x_3 = f\left(x_1, x_2\right) \tag{2.1}$$

To reduce the dimensionality of the equations that we are going to solve, we want to describe the surface using only 2 variables. That is, we can use the parameterization

$$x_i^{\circ} = x_i^{\circ}(\eta_1, \eta_2) \tag{2.2}$$

where x_i^0 are the Cartesian components of the position of a point on the surface.

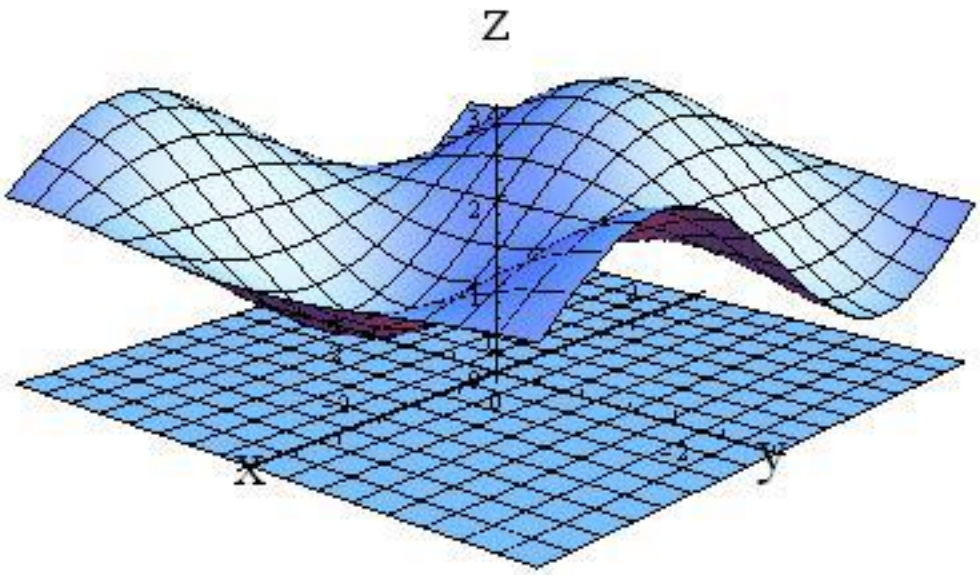

Figure 2: A mapping of a 2D surface onto a 3D parametric surface.

Considering a curve $\eta_1 = \eta_1(t)$, $\eta_2 = \eta_2(t)$ in the parametric domain of the surface, then $x_i^\circ = x_i^\circ(t) = x_i^\circ(\eta_1(t), \eta_2(t))$ is a parametric curve lying on the surface.

Defining

$$s_i^\circ = \frac{\partial x_i^\circ}{\partial \eta_1} \quad \text{and} \quad t_i^\circ = \frac{\partial x_i^\circ}{\partial \eta_2} \tag{2.3}$$

These are two tangent vectors to the plane such that

$$\dot{x}_i^\circ(t) = s_i^\circ \dot{\eta}_1 + t_i^\circ \dot{\eta}_2 \tag{2.4}$$

The surface normal vector is perpendicular to the tangent plane and hence the unit normal vector is given by the cross product of these two tangent vectors divided by its absolute value.

$$n_i^{\circ} = \frac{\epsilon_{ijk} s_j^{\circ} t_k^{\circ}}{\left| \epsilon_{ijk} s_j^{\circ} t_k^{\circ} \right|} \tag{2.5}$$

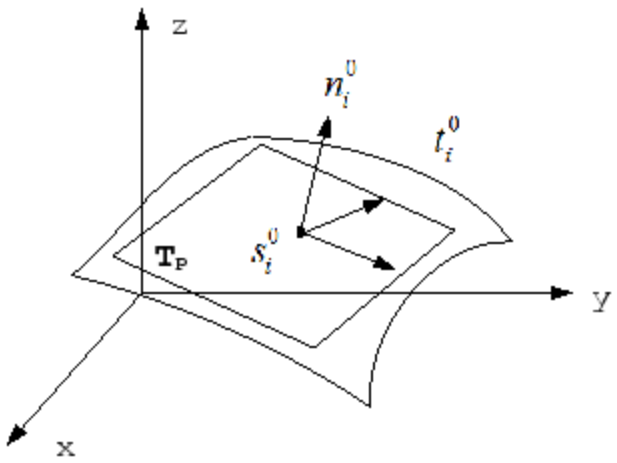

Figure 3: A scematic of the representation for the normal to the point on a surface.

Within the model equations the surface gradient and divergence operators will appear, and so we will need a description of these as well. For a surface in a scalar field, components of the surface gradient is given as

$$\begin{aligned} \nabla_j^s &= -\epsilon_{jkm} n_k^0 D_m \\ &= \frac{\partial}{\partial x_j} - n_j^0 n_l^0 \frac{\partial}{\partial x_l} \end{aligned} \tag{2.6}$$

where D_j is a tangential surface operator

$$D_j = n_i^0 \epsilon_{ikj} \frac{\partial}{\partial x_k} = \frac{1}{\left| \vec{s^0} \times \vec{t^0} \right|} (t_j^0 \frac{\partial}{\partial \eta_1} - s_j^0 \frac{\partial}{\partial \eta_2}) \tag{2.7}$$

Chapter 3: Governing Equations

In this section we will motivate the equations used to model the organogenesis process. We first use a simple one-dimensional picture, and then generalize to the full theory.

3.1 Simple 1D Description

Consider a flat layer of cells as shown in Figure 4. Initially the cell layer is dormant, but the cells on the left side are triggered to grow. These cells begin to deposit mineral and move normal to the plane that they are sitting upon. This movement causes a separation between these cells and those in front of them, which in turn triggers these cells to begin depositing mineral. This process is the basic picture of how the commencement front propagates. As the commencement front passes by, cells begin to migrate at a velocity v_0 in the normal direction to the DEJ. The cells behind the commencement front are no longer in the same positions that they were prior and so they will also move in the plane in order to attain a more favorable arrangement, e.g. one in which the spacing between neighbors is more favorable. This rearrangement causes a lateral velocity component within the plane of the cell sheet v_f to happen. Unlike the normal component which is driven by the rate at which the cells secrete mineral, the lateral component changes continuously and can set up wave-like behaviors owing to the strain change propagating through the cell sheet. Figure 4 is a one-dimensional illustration of this process. Each point along the surface grows vertically after it is triggered and moves smoothly in the normal direction while a wavelike in-plane rearrangement with a wave magnitude u_s can occur due to the cell response to time-varying surface strains.

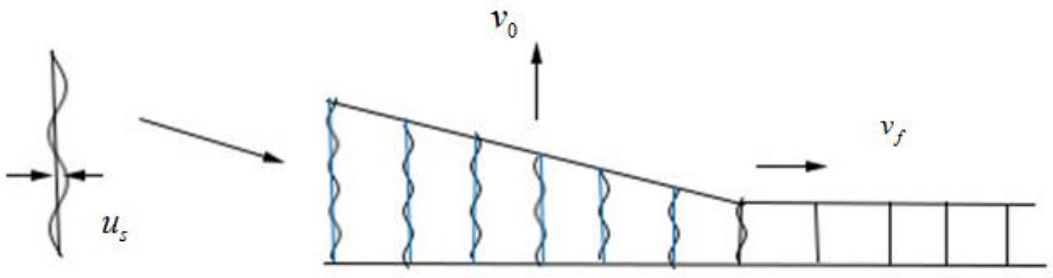

Figure 4: In-plane and out-of-plane motion in a 1D space.

3.2 Phase-field Description for the Commencement Front

To track the location of the commencement front, an independent variable ϕ is introduced. The parameter ϕ is used to differentiate between secretory, $\phi = 1$ and non-secretory cells $\phi = 0$. In phase-field terminology ϕ is called an order parameter and is used as a configurational variable that enters the description of a free energy. In this work we will use such a free energy, although this does not hold any physical significance and the parameters of the model will be chosen such that the energy barriers associated with the free energy will be easily overwhelmed by the driving forces associated with the cell kinematics. Effectively, the phase-field equation will be used to track the location of the commencement front.

The derivation of the governing equation for the order parameter will follow the work (and wording) of Fried and Gurtin [23-25]. We introduce a micro-force vector with components ξ_i such that $\xi_i m_i \phi$ (m_i is the unit outward normal vector to the surface edge) represents a power density expended across surface edges by neighboring cells, an internal micro-force vector π such that $\pi\phi$ is the power density transmitted by the

cells internally, and an external micro-force vector γ such that $\gamma\phi$ is a power density expended on the cells by external sources. Usually ξ_i and π are related to ϕ via thermodynamic or energetic constitutive relationships. Here we will follow this prescription but note that the relationship to the physics for this problem is tenuous, and the objective is simply to use this approach to locate the position of the commencement front. We will attempt to motivate this further once the governing equations are derived.

It is now assumed that there is an overall balance of these micro-forces such that,

$$\int_{\partial S} \xi_i m_i d\Gamma + \int_S (\pi + \gamma) dS = 0 \tag{3.1}$$

Defining e_i^S as the unit vector tangent to ∂S, then we can use the surface divergence theorem for the first term as,

$$\begin{aligned} \int_{\partial S} \xi_i m_i dS &= \int_{\partial S} \xi_i \epsilon_{ijk} e_j^s n_k dS \\ &= \int_S n_p \epsilon_{pqj} \epsilon_{ijk} (\xi_i n_k)_{,q} dS \\ &= \int_S D_j (\epsilon_{jki} \xi_i n_k) dS \\ &= \int_S \nabla_i^s \xi_i dS \end{aligned} \tag{3.2}$$

Now we have

$$\nabla_i^s \xi_i + \pi + \gamma = 0 \quad \text{in S} \tag{3.3}$$

This is the point-wise micro-force balance governing the evolution of the order parameter ϕ. We will not go through the details here, but following prior work it can be shown that the constitutive law for the order parameter and its gradient can be derived from a free energy potential as,

$$\xi_i = \frac{\partial \psi}{\partial(\nabla_i^s \phi)} \quad \text{and} \quad \pi = -\frac{\partial \psi}{\partial \phi} - \beta \dot{\phi} \tag{3.4}$$

Here β is a "viscosity" that controls the rate at which the order parameter can respond to changes in the overall set of internal and external micro-forces acting at that point. Next, it is assumed that the free energy of the cells takes the following form

$$\psi(\phi, \nabla_i^s \phi) = \frac{a_\circ}{2} \left| \nabla_i^s \phi \right|^2 + a_1 \phi^2 (1-\phi)^2 \tag{3.5}$$

The first term of this energy function penalizes sharp gradients in the order parameter, which will give the commencement front a finite thickness instead of allowing it to be a sharp interface. Again, the primary purpose for this approach is to make the computation of the location and evolution of the commencement front more tractable. Next, the second term of this free energy is a simple double-well potential and is illustrated in Figure 5. Here the goal is to give the order parameter to distinct states in which it will preferentially reside. In other words, when $\phi = 0$ the cells are non-secretory and thus not migrating normal to the DEJ surface, and when $\phi = 1$ the cells are secreting and moving with its component of velocity normal to the DEJ surface at a constant v_0. Again, without the smoothing gradient term the micro-force balance equation would only allow the order parameter to reside in one of these two states (at

least in the absence of other external forcings) and the commencement front boundary would be sharp. The gradient term allows a smooth transition between the secretory and non-secretory states within a small region. Physically we can take this length scale to be of the order of the size of a cell.

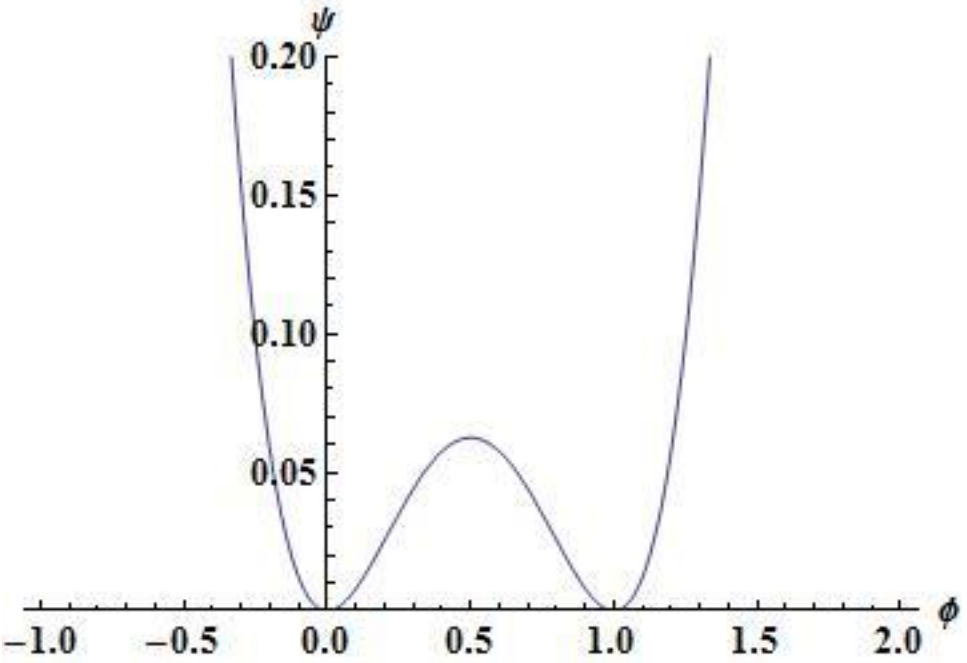

Figure 5: The free energy distribution as a function of ϕ.

With this free energy we can now compute the set of micro-forces as,

$$\xi_i = \frac{\partial \psi}{\partial \nabla_i^s \phi} = a_\circ \nabla_i^s \phi \tag{3.6}$$

$$\pi = -\beta \dot{\phi} - \frac{\partial \psi}{\partial \phi} = -\beta \frac{\partial \phi}{\partial t} - a_1 [2\phi(1-\phi)^2 - 2\phi^2 (1-\phi)]. \tag{3.7}$$

Additionally we must specify the external driving force γ. Here we have a great deal of flexibility with the goal of reproducing the physical behaviors seen in cell populations. The question to be addressed is, what is the signal or cue that tells a dormant cell to start secreting? There are several postulates that can be made and studied. The basic assumption that is made by Cox [6, 18] is that the cells will respond when they sense a change in their local environment associated with the relative changes in positions of its neighbors. Here we will assume that the relative shear strain caused near the commencement front will trigger the cells in front of it to begin secreting. Hence, we take the external micro-force to be of the form,

$$\gamma = c_0 \varepsilon_s (1-\phi) \tag{3.8}$$

Here,

$$\varepsilon_s = \sqrt{\frac{\partial u_i n_i^{\circ}}{\partial \eta_\alpha} \frac{\partial u_j n_j^{\circ}}{\partial \eta_\alpha}} \tag{3.9}$$

is the effective shear strain, and note that there is summation over i and j from 1 to 3, and over α from 1 to 2. Also notice that this term is "turned off" once the cells are fully behind the commencement front where $\phi = 1$. Finally, the parameter c_0 represents the strength of this driving force. Collecting all of these terms then provides us with the following micro-force balance equation governing the evolution of the order parameter,

$$a_0 D_j [D_j \phi - n_j n_k D_k \phi] - 2a_1 \phi (1-\phi)(1-2\phi) + c_0 \varepsilon_s (1-\phi) = \beta \frac{\partial \phi}{\partial t} \quad . \tag{3.10}$$

3.3 Kinematics and In-plane Kinetic Equations

We now proceed to the description of the kinematics of the cell layer and then postulate a set of kinetic equations governing the in-plane motions of the cells. First, the normal distance of the growth front from the DEJ, which is also the thickness of the accumulated enamel, is calculated as

$$u_i n_i^0 = v_0 (t - t_c(x_i^0)) \tag{3.11}$$

where t is the time and $t_c(x_i^0)$ is the time when the commencement front passes through the location of the original DEJ boundary x_i^0. This equation shows that in the normal direction, dental enamel is deposited with the constant velocity v_0. Given that we are not tracking the commencement front explicitly, but instead using the order parameter ϕ, we need to rewrite this equation in terms of ϕ. This is accomplished by recognizing that the normal velocity should vanish when $\phi = 0$ and should equal v_0 when $\phi = 1$.

$$u_i n_i^0 = v_0 \int_0^t f(\phi) dt \tag{3.12}$$

where $f(\phi) = 0$ when $\phi = 0$, and $f(\phi) = 1$ when $\phi = 1$. In this report, we will assume that $f(\phi) = \phi^2$. By differentiating (3.13) we can obtain the equation for the normal velocity as,

$$\frac{du_i}{dt} n_i^0 = v_0 \phi^2 \tag{3.13}$$

Here u_i are the displacements of the cells. We note that this motion of the cells normal to the DEJ surface will cause in-plane stretching of the cell sheet, which in turn will cause the cells to want to rearrange in order to offset this disturbance in their local environment. Hence, it is useful to derive some additional kinematic relationships for the cell sheet.

The new locations of points on the surface are given as,

$$x_i = x_i^0 + u_i = x_i^0 + n_i v_0 \int_0^t f(\phi) dt + u_i^s \quad . \tag{3.14}$$

Here $u_i^s = u_i - u_j n_j n_i$ is the surface displacement of the cells, i.e. the tangential displacement within the growth surface. With this description of the new locations of the surface points, we now proceed to determining the deformation gradients associated with this deformation.

$$F_{i\alpha} \equiv \frac{\partial x_i}{\partial \eta_\alpha} = \frac{\partial x_i^0}{\partial \eta_\alpha} + v_0 \int_0^t f(\phi) dt \frac{\partial n_i^0}{\partial \eta_\alpha} + v_f \int_0^t \frac{df}{d\phi} n_i^0 \frac{\partial \phi}{\partial \eta_\alpha} dt + \frac{\partial u_i^s}{\partial \eta_\alpha} \tag{3.15}$$

This in-plane deformation gradient can be used to generate surface strain measures. For example, a surface Green-Lagrange strain can be defined by considering the change in the square of the arc length of segments on the surface,

$$\frac{1}{2}(ds^2 - ds_0^2) = \frac{1}{2}(F_{i\alpha} F_{i\beta} - \frac{\partial x_i^0}{\partial \eta_\alpha} \frac{\partial x_i^0}{\partial \eta_\beta}) d\eta_\alpha d\eta_\beta = E_{\alpha\beta} d\eta_\alpha d\eta_\beta \tag{3.16}$$

In this report we will use gradients of the area strain at a point in order to drive in-plane motions of the cells. Of course more general deformation measures can be implemented, but for simplicity we investigate the area strain first. The area strain in the surface is,

$$\varepsilon = \sqrt{1 + 2E_{\gamma\gamma} + 4\det(\underset{\sim}{E})} - 1 \quad . \tag{3.17}$$

Now we introduce a kinetic assumption for the in-plane motion of the cells. The assumption is motivated by the physical consideration that the cells have a favorable spacing that they would like to maintain with their neighbors. Therefore, if a cell feels compressed on its left side and extended on its right side it will move to the right in order to "equilibrate" this difference. Also, from private communications with Dr. Brian Cox, in-plane cell motions can take on the appearance of wave-like behavior and hence instead of simply relating cell velocity to the strain gradient, we will relate the cell acceleration to the strain gradient. This leads us to our assumed form for the kinetics governing the in-plane cell motions,

$$\frac{\partial^2 u_i^s}{\partial t^2} = \kappa \nabla_i^s \varepsilon \tag{3.18}$$

Here again u_i^s are the in-plane components of u_i. Note that this equation has the form of a wave equation with second time derivation of the displacements on the left and second spatial derivatives of the displacements on the right. We do note that this equation is not associated with the mass inertia of the cells as the momentum of the cells during

these motions is exceedingly small in comparison to the forces that they can generate to affect their motions.

Chapter 4: Finite Element Formulation

The governing equations for the phase-field model are Eqs. (3.5) – (3.10), (3.13) and (3.16) – (3.18). To solve these equations using finite element method, we identify the order parameter ϕ and the displacements u_i to be used as nodal degrees of freedom. Furthermore, instead of a fully couple scheme we use a staggered method to solve the coupled equations. Specifically, for a given distribution of the displacements we solve the micro-force balance over a time increment for the updated values of the order parameter, and then for this new distribution of the order parameter, we solve for updated distributions of the nodal displacements. Each of the field quantities are interpolated by the nodal quantities through the same set of shape functions such that

$$\phi(\eta_1,\eta_2)=\sum_M N^M(\eta_1,\eta_2)\,\phi^M \tag{4.1}$$

$$u_i(\eta_1,\eta_2)=\sum_M N^M(\eta_1,\eta_2)\,u_i^M \tag{4.2}$$

All of the requirements for standard C0 continuous elements [27] must be satisfied for the shape functions. Therefore, the strains and gradients of ϕ may still have jumps in certain components along element boundaries, but the relative displacements and ϕ are approximated by continuous functions.

The principle of virtual work for the micro-force balance equation can be written as,

$$\int_S(\epsilon_{ijk}n_k\xi_i D_j\delta\phi+\mu\delta\phi+\beta\dot{\phi}\delta\phi)dS=\int_{\partial S}\xi_i m_i\delta\phi dS+\int_S c_0\varepsilon_s(1-\phi)\delta\phi dS \tag{4.3}$$

where we have defined the quantity $\mu = \frac{\partial \psi}{\partial \phi}$. To integrate numerically through time, we will use a simple forward Euler scheme for the time integration such that the time rate of the order parameter is approximated as $\dot{\phi} = \frac{\phi - \phi^{t-\Delta t}}{\Delta t}$.

Implementing the shape functions and their associated spatial derivatives, (4.3) becomes

$$\int_S (\delta\phi^N B_j^N \epsilon_{ijk} n_k \xi_i + \delta\phi^N N^N (\mu - c_0 \varepsilon_s (1-\phi) + \frac{\beta}{\Delta t}\phi))dS = \int_{\partial S} \delta\phi^N N^N \xi_i m_i dS \quad (4.4)$$

where summation is implied over the repeated superscripts and the repeated subscripts, and the surface derivatives of the shape functions are given by,

$$B_i^M = D_i N^M \quad (4.5)$$

After expanding the equations by recognizing that the $\delta\phi^N$ are arbitrary, equation (4.4) represents a nonlinear set of algebraic equations that must be solved for each time increment. With a known set of all nodal degrees of freedom at time t, the equations can be written in compact form as,

$$\mathbf{P}\left(\mathbf{d}^{t+\Delta t}\right) = \mathbf{F} \quad (4.6)$$

These equations are solved with the Newton–Raphson method:

$$\left.\frac{\partial \mathbf{P}}{\partial \mathbf{d}}\right|_{\mathbf{d}_\mathbf{i}^{t+\Delta t}} \Delta \mathbf{d}_\mathbf{i} = \mathbf{F} - \mathbf{P}\left(\mathbf{d}_\mathbf{i}^{t+\Delta t}\right) \quad (4.7)$$

where i represents the current iterate in the Newton–Raphson sequence and $\Delta\mathbf{d}_i$ is the increment computed for $\mathbf{d}_i^{t+\Delta t}$ such that $\mathbf{d}_i^{t+\Delta t} = \mathbf{d}_{i-1}^{t+\Delta t} + \Delta\mathbf{d}_i$. Note that the first term of Eq. (4.7) is the Newton–Raphson Jacobian matrix, which is symmetric. The Newton–Raphson procedure is carried out until a suitable level of convergence is obtained. Thus a solution for the order parameter fields at time step $t + \Delta t$ is solved. For completeness the finite element Jacobian matrix for the micro-force balance can be derive from (4.4) as:

$$\begin{aligned} & d\int_S \delta\phi^N [B_j^N \epsilon_{ijk} n_k \xi_i + N^N (\mu - c_0 \varepsilon_s (1-\phi) + \frac{\beta}{\Delta t}\phi)] dS \\ &= \int_S \delta\phi^N [B_j^N \epsilon_{ijk} n_k \frac{\partial \xi_i}{\partial \nabla_p^s \phi} \epsilon_{plm} n_m B_l^M d\phi^M + N^N (\frac{\partial \mu}{\partial \phi} + c_0 \varepsilon_s + \frac{\beta}{\Delta t}) N^M d\phi^M] dS \\ &= \delta\phi^N K^{NM} d\phi^M \end{aligned} \tag{4.8}$$

For the in-plane kinetics, Equation (3.18) can be cast as the following variational statement.

$$\int_S \frac{\partial^2 u_i^s}{\partial t^2} \delta u_i^s dS = \int_S \kappa \nabla_i^s \varepsilon \delta u_i^s dS \tag{4.9}$$

Where

$$\delta u_i^s = u_i - u_j n_i^\circ n_j^\circ = A_{ij}^s u_j \tag{4.10}$$

Introducing the finite element interpolations, the left hand side is,

$$\int_S \frac{\partial^2 u_i^s}{\partial t^2} \delta u_i^s dS = \int_S \delta u_l^N N^N A_{il}^s A_{ij}^s N^M \frac{v_j^{t+\Delta t}_M - v_j^t_M}{\Delta t} dS \tag{4.11}$$

where

$$v_j^{t+\Delta t}_M = \frac{u_j^{t+\Delta t}_M - u_j^t_M}{\Delta t} \tag{4.12}$$

and the right hand side is,

$$\begin{aligned} &\int_S \kappa \nabla_i^s \varepsilon \delta u_i^s dS \\ &= -\int_S \delta u_l^N A_{il}^s B_j^N \epsilon_{ijk} n_k \varepsilon \kappa dS \quad . \\ &= -\delta u_l^N \{F_l^N\} \end{aligned} \tag{4.13}$$

Defining,

$$\int_S \delta u_l^N N^N A_{il}^s A_{ij}^s N^M v_j^t_M dS = \delta u_l^N \{F_v^N\} \tag{4.14}$$

the finite element equation for the in-plane displacements becomes,

$$\int_S \delta u_l^N N^N A_{il}^s A_{ij}^s N^M v_j^{t+\Delta t}_M dS = -\delta u_l^N (\{F_l^N\}\Delta t + \{F_v^N\}) \tag{4.15}$$

The normal velocity equation is then included to enforce the constraint on the total velocity that it imposes as,

$$\int_S \frac{du_j}{dt} n_j^0 \delta u_n dS = \int_S v_0 \phi^2 \delta u_n dS \tag{4.16}$$

$$\int_S \delta u_i^N N^N n_i^0 n_j^0 N^M v_j^M dS = \int_S \delta u_i^N N^N n_i^0 v_0 \phi^2 dS \tag{4.17}$$

Adding the in-plane and normal equations together, we can obtain the entire stiffness and force matrices for the cell dynamics. The equations governing the updated displacement quantities are linear and hence a single solution step is sufficient without the need for the Newton-Raphson method.

Chapter 5: Results

In this section we will present some basic numerical results from the model and finite element method, and discuss some of the issues encountered involving boundary conditions.

5.1 Uncoupled Phase-field Solutions

Here we present fundamental solutions to the phase-field equation in both one dimension on a flat surface and on a curved surface representative of the DEJ. See section 5.5 for a detailed mathematical description of the DEJ surface. These uncoupled solutions are shown here in order to provide an illustration of the structure of the commencement front as it is described with the phase-field method.

Figure 6 shows a simple one-dimensional solution for the commencement front for the following set of parameters, $a_0 = 0.04$, $a_1 = 1$, $c_0 = 0$, $v_0 = 1$, $\beta = 0$ and $\kappa = 0$. The solution clearly illustrates the internal boundary layer where the order parameter changes abruptly from 1 to 0 representing the smoothed location of the commencement front.

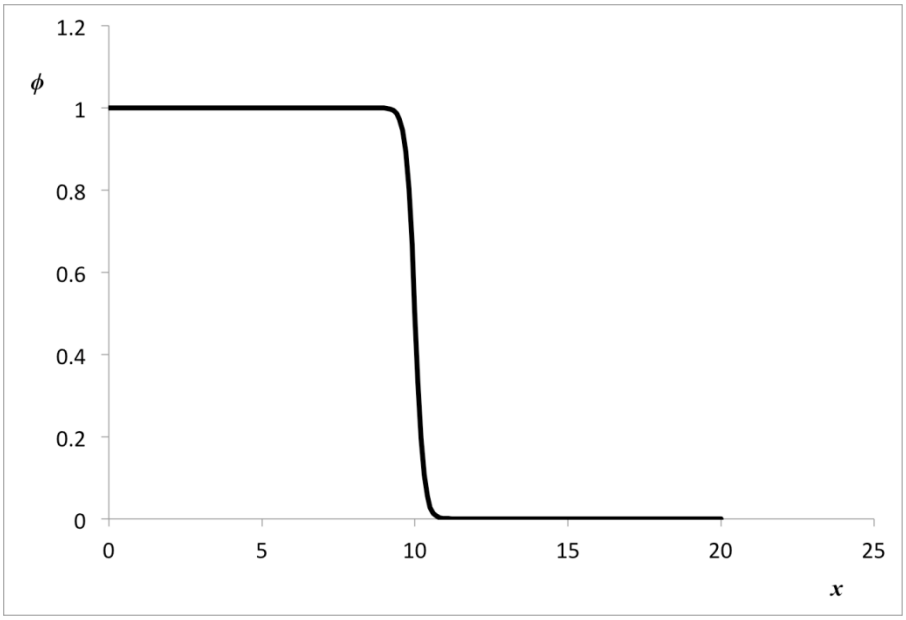

Figure 6: An illustration of the commencement front evolution of a flat surface.

Figure 7 is a contour plot of the phase-field order parameter on the curved DEJ surface. This solution illustrates the ability of the numerical method to produce solutions on curved surfaces as well as how features of the commencement front are affected by such curvatures. Note that on a flat surface the phase-field solution for the commencement front would result in a straight vertical boundary.

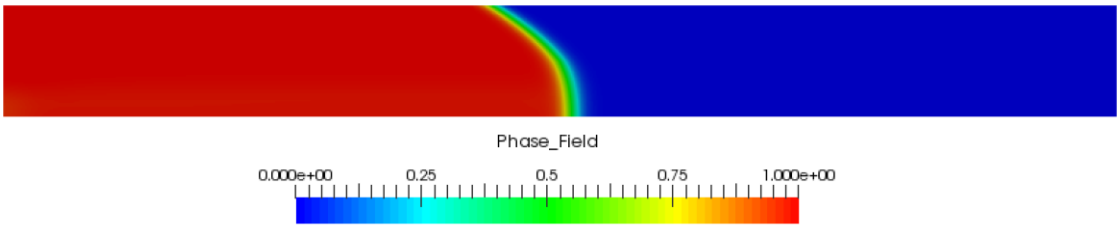

Figure 7: A contour plot of the phase-field order parameter representing the commencement front on a curved surface.

5.2 Boundary conditions

In this section we investigate some simple solutions of the in-plane kinetics equations. One feature that was not discussed in the presentation of the theory was the boundary conditions that are necessary to provide meaningful solutions for the in-plane motions. Without appropriate boundary conditions, equation (3.18) tends to drive the area strain towards zero. This means that as the cells begin to migrate in the normal direction, or if they are simply given an in-plane stretch in one direction, then there is a relatively strong "force" that causes the cells to want to migrate in from the other directions in order to maintain a constant area. This behavior may be a deficiency in the description of the cell kinetics. However, in this report we will simply attempt to control this behavior by enforcing conditions on the boundaries that constrain the cells on the boundaries to remain on the boundary curve which can be translated in the normal direction to its initial state in accordance with the normal displacements associated with normal growth of the enamel. This means that secretory-stage ameloblasts always remain on the smooth surface of the enamel formed up to that time [4]. That is, cells are constrained to lie on the current growth front and move normal to the growth front line to form a smooth two-dimensional curved sheet. Thus, the constraining effect of the enamel surface plays an important role in amelogenesis.

Therefore, our equations for this constraint is written as

$$u_i t_i = 0 \tag{5.1}$$

Where, if s_i represents the unit vector that is tangential to the sheet boundary then $t_i = \epsilon_{ijk} n_j s_k$ is the unit vector that is both in the plane of the sheet and normal to the sheet boundary. Hence, cells on the edge of the sheet can only in the normal direction to the

sheet and along the edge direction of the sheet. Additionally, in the simulations presented in this report, the sheet surface is fixed at one edge in the normal direction as well, i.e.

$$u_i n_i = 0 \quad , \tag{5.2}$$

otherwise the possibility of negative normal displacements arises.

Figure 8 and Figure 9 are generated on a simple flat sheet that was given an initial stretch of the entire cell sheet in the *x*-direction, and at time $t = 0$ was released. The resulting solution should look like a vibrating bar. Figures 8 and 9 are the *x*-displacement at the center of the edge of the sheet that was fully released. The opposite edge was held fixed with zero displacement. Figure 8 shows the behavior for the case with the constraints that the edge cells cannot move in the in-plane normal direction. There is a clear wave phenomenon for the in-plane movement with oscillations of the free edge in a fashion similar to a vibrating bar. However, if the edge of the strip is left without constraints, motion becomes some combination of waves traveling in the stretch direction and transverse to the direction leading to a behavior that is not representative of those that we want to capture for cell sheets.

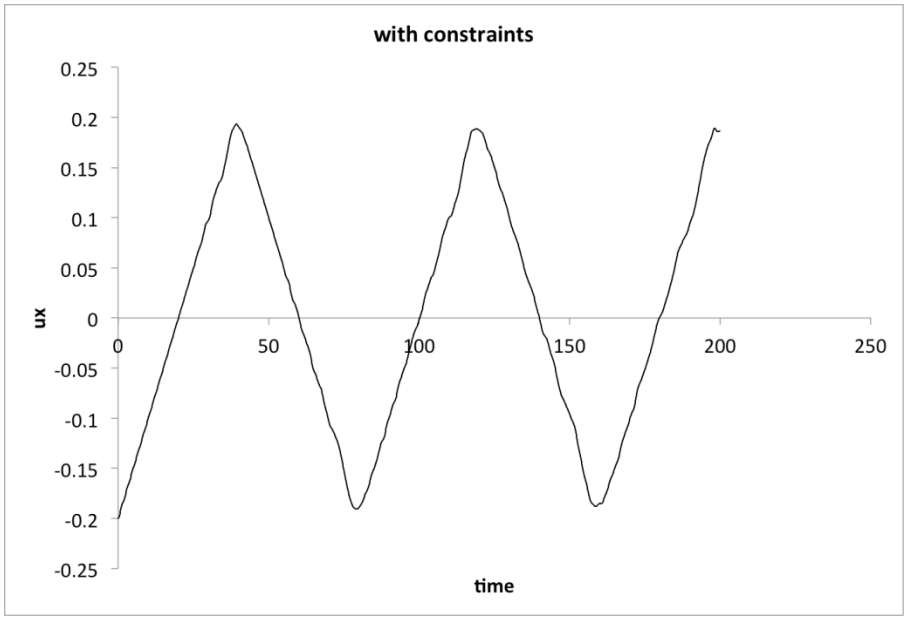

Figure 8: Longitudinal displacement of the middle of the left edge on the flat surface after releasing the left side at a certain value with boundary conditions.

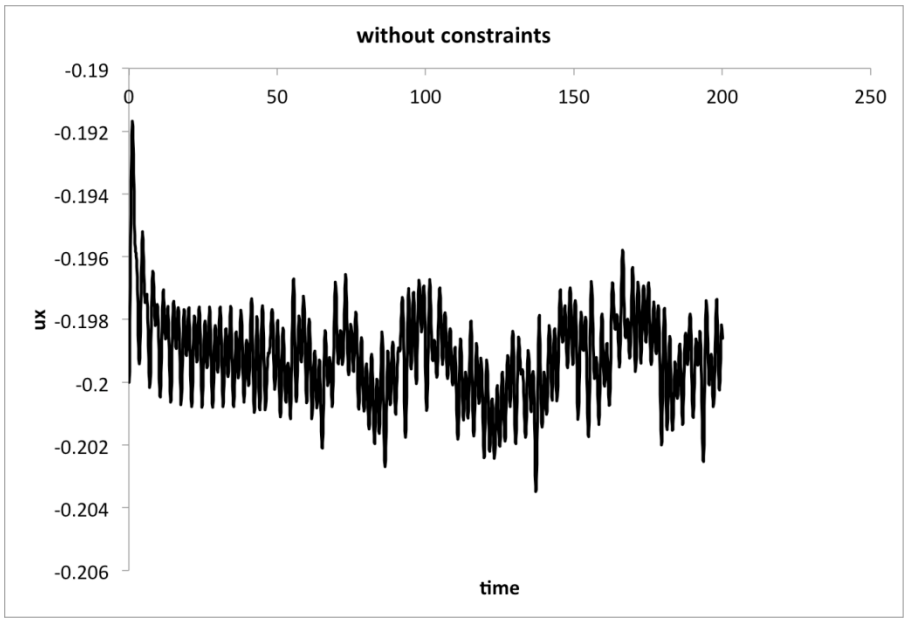

Figure 9: Longitudinal displacement of the middle of the left edge on the flat surface after releasing the left side at a certain value without boundary conditions.

5.3 Parameter Study for the Behavior on a Flat Surface

In the model there are 6 parameters: a_0, a_1, c_0, v_0, β and κ. In reduce the parameter space, we normalize our governing equations and find a reduced set of parameters. First, we analyze the phase-field equation (3.10),

$$\frac{a_\circ}{a_1} D_j[D_j\phi - n_j n_k D_k\phi] - 2\phi(1-\phi)(1-2\phi) + \frac{c_\circ}{a_1}\varepsilon_s(1-\phi) = \frac{\beta}{a_1}\frac{\partial\phi}{\partial t} \tag{5.3}$$

Then we can simplify parameters by defining the characteristic time scale,

$$t_0 = \frac{\beta}{a_1} \tag{5.4}$$

the characteristic length scale,

$$l_0 = \sqrt{\frac{a_0}{a_1}} \tag{5.5}$$

the characteristic strain scale,

$$\varepsilon_0 = \frac{c_0}{a_1} \tag{5.6}$$

and the characteristic velocity scale,

$$v_0 = \frac{l_0}{t_0} = \frac{\sqrt{a_0 a_1}}{\beta} \tag{5.7}$$

Now, the two kinetic equations (3.13) and (3.18) can also be normalized as

$$\overline{v_n} = \frac{v_0 t_0}{l_0}\phi^2 \tag{5.8}$$

$$\frac{d\overline{v_i^s}}{d\bar{t}} = \frac{\kappa t_0^2}{l_0^2}\overline{\nabla_i^s \varepsilon} \tag{5.9}$$

where $\bar{v} = \frac{v}{v_0}$, $\bar{t} = \frac{t}{t_0}$, $\overline{\nabla_i^s \varepsilon} \sim \frac{d\varepsilon}{d\bar{x}} = \frac{d\varepsilon}{dx / l_0}$.

Thus, there are only three independent parameters left, which are c_0, v_0 and κ. To begin, we choose the flat surface to test how these parameters will affect results and also to determine appropriate values of these three parameters for simulations on the curved surface. We set the surface of all cases to be a $50l_0 \times l_0$ long strip with 500 elements in the length direction and 10 elements in the width direction. The parameter values and results for the maximum area strain, distance to the commencement front divided by the normal displacement of the left edge, and maximum in-plane displacement as the front reaches the end of the cell layer are as shown in Table 1.

Table 1: Different sets of parameter values and the corresponding results.

Case	c_0	v_0	κ	maximum strain	x_f / u_z	$u_x^{\max}$
1	1	0.01	1e-6	1.5%	5.99	1e-3
2	10	0.01	1e-6	0.17%	17.7	5e-6
3	1	0.1	1e-6	15%	1.82	5e-4
4	1	0.01	1e-4	1.53%	5.99	1e-2

As Table 1 shows, four sets of parameter values have been analyzed to study the effect of these three parameters by first setting $c_0 = 1$, $v_0 = 1e-2$ and $\kappa = 1e-6$ and then changing one parameter of the set while keep the other 2 at the same value. We also compare the features of 4 time instance when commencement front moves 10, 20, 30 and $40 l_0$. Note that x_f stands for the location of the commencement front. u_z is the normal displacement of the left side of the cell sheet, and $u_x^{\max}$ is the maximum in-plane displacement within the sheet when the front nears the right side of the sheet.

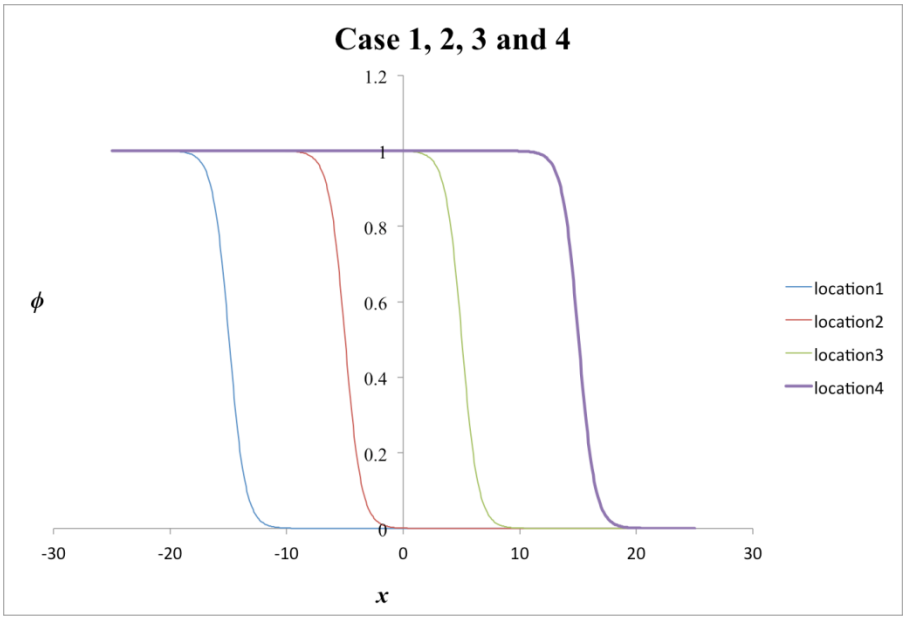

Figure 10: Phase-field plot indicating the location of the commencement front at 4 times for a flat surface.

As mentioned above, the locations of the commencement front at 4 time instances when it moves 10, 20, 30 and $40\,l_0$ are shown in Figure 10. Again, for secretory cells $\phi = 1$ while non-secretory cells have $\phi = 0$.

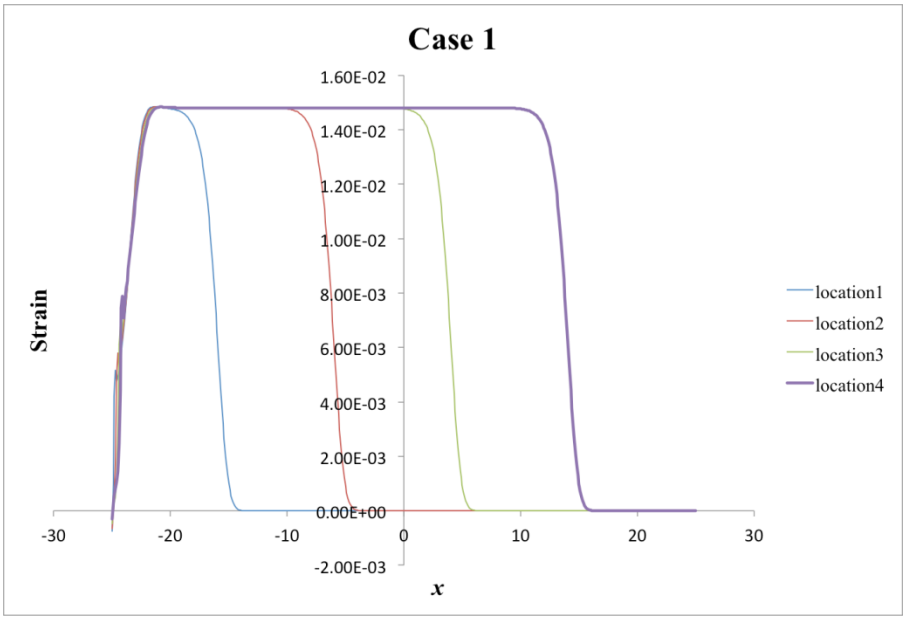

Figure 11: Strain plot for Case 1 at the 4 front locations.

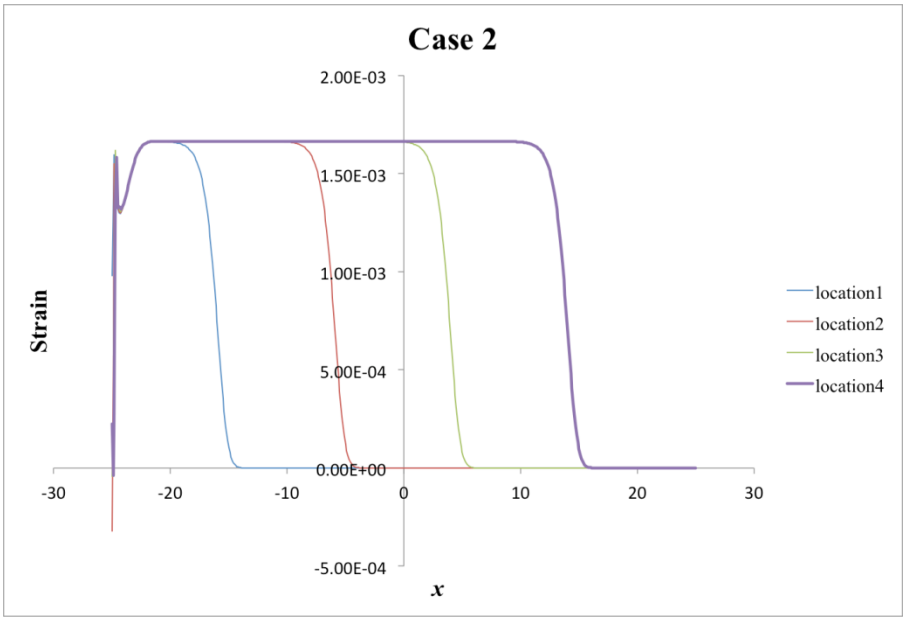

Figure 12: Strain plot for Case 2 at the 4 front locations.

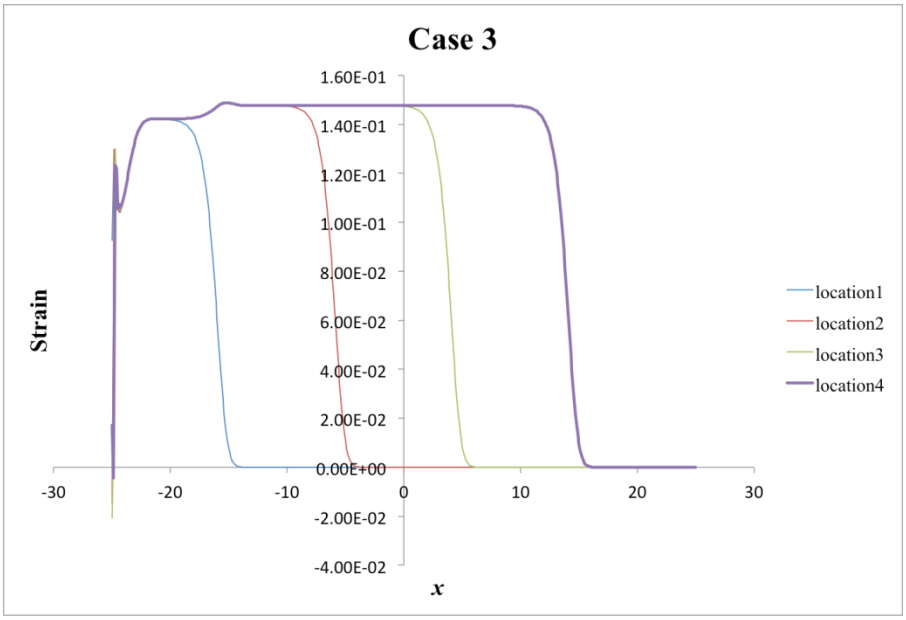

Figure 13: Strain plot for Case 3 at the 4 front locations.

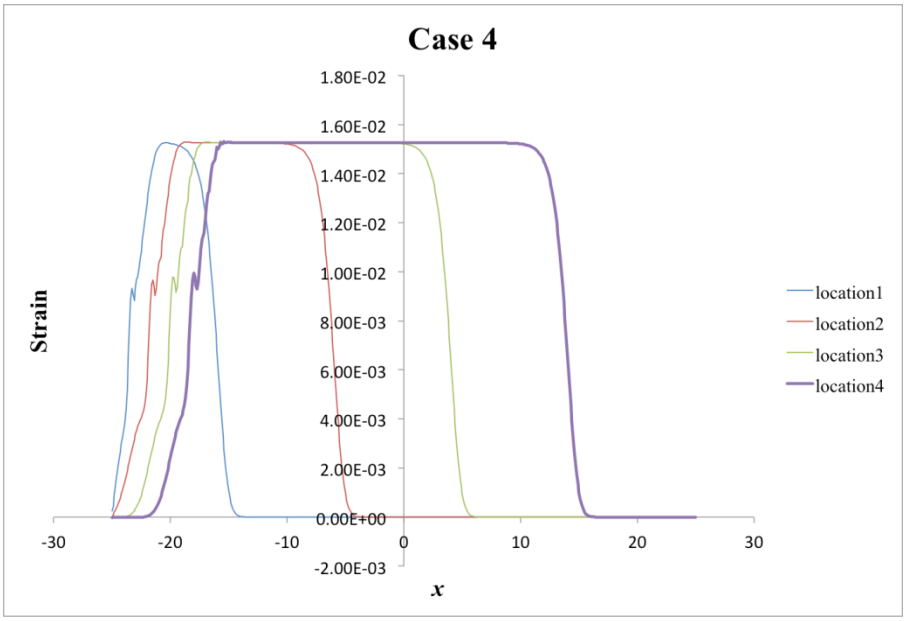

Figure 14: Strain plot for Case 4 at the 4 front locations.

Figures 11-14 shows how the strain for each of the cases changes through time. From the left side to commencement front, the area strain of the cell sheet grows initially during the propagation and reaches a maximum value of 1.5%, 0.17%, 15% and 1.53% for each case. As time goes on, more cells will obtain the maximum strain. Maximum strains for Cases 1 and 4 are similar, from which we can infer that the ratio c_0 / v_0 plays a significant role in determining the strain rather than c_0 or v_0 themselves, and κ appears to have a minor effect on the area strain. Then from Cases 2 and 3 we can see that when the c_0 / v_0 ratio increases, the maximum strain decreases.

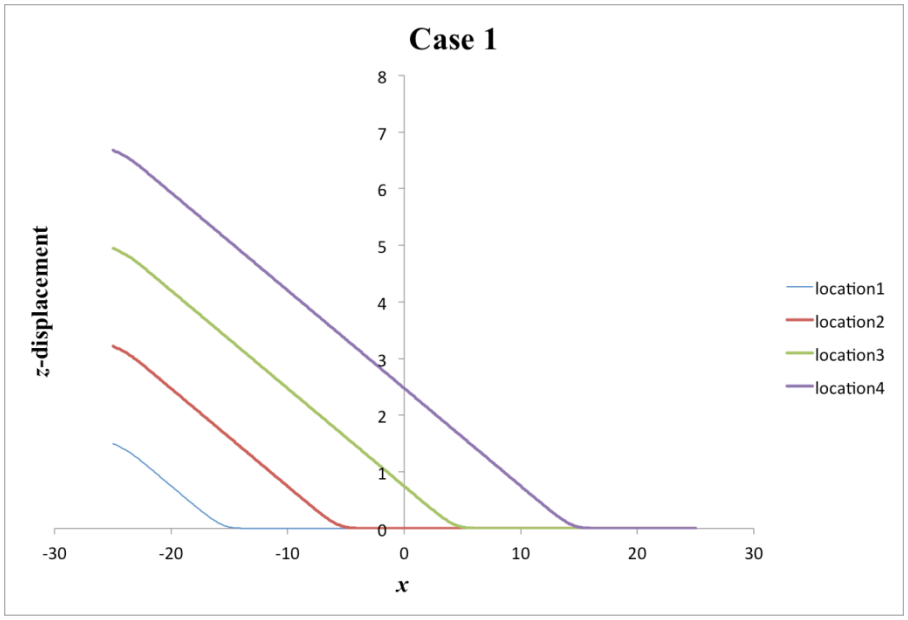

Figure 15: *Z*-displacement plot for Case 1 at the 4 front locations.

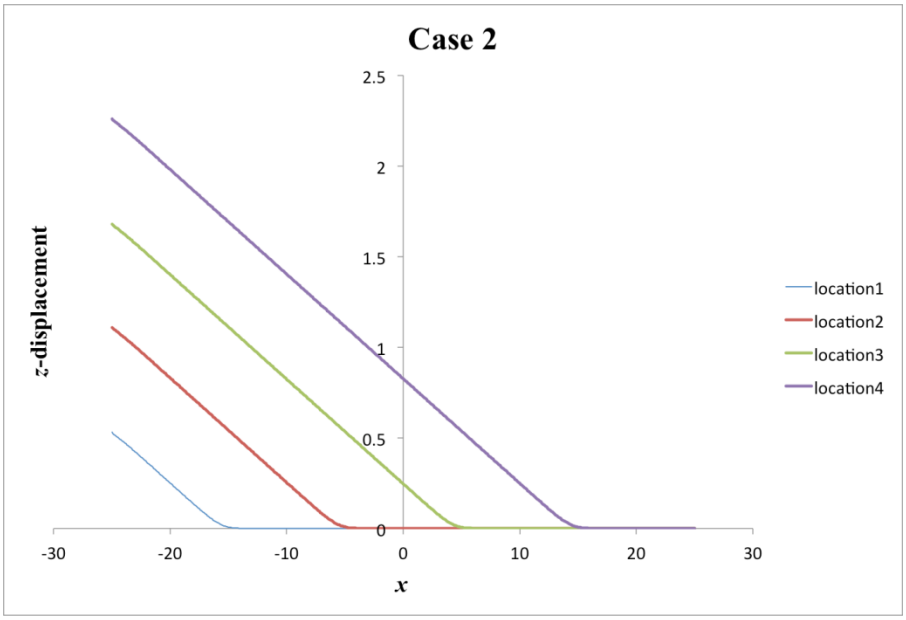

Figure 16: *Z*-displacement plot for Case 2 at the 4 front locations.

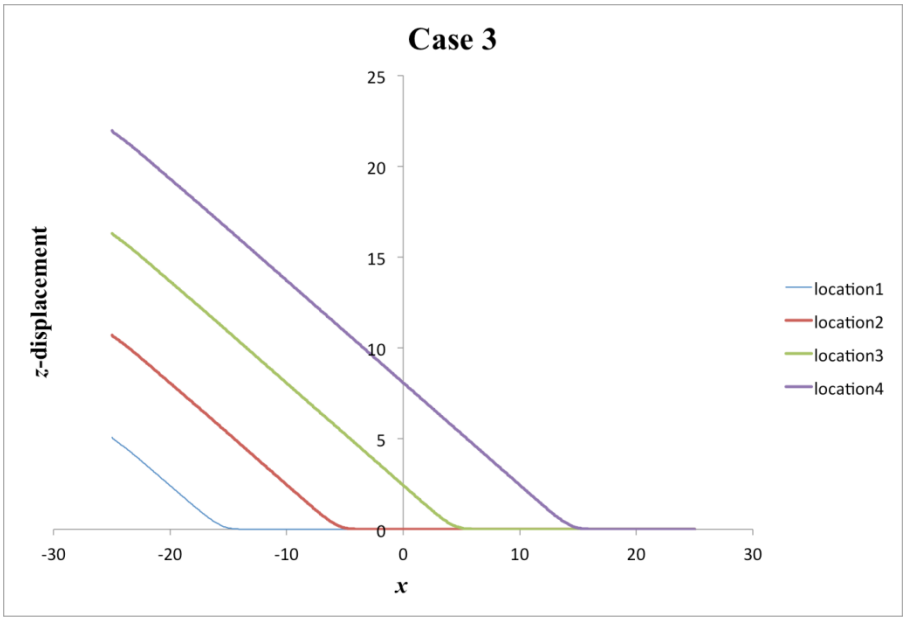

Figure 17: *Z*-displacement plot for Case 3 at the 4 front locations.

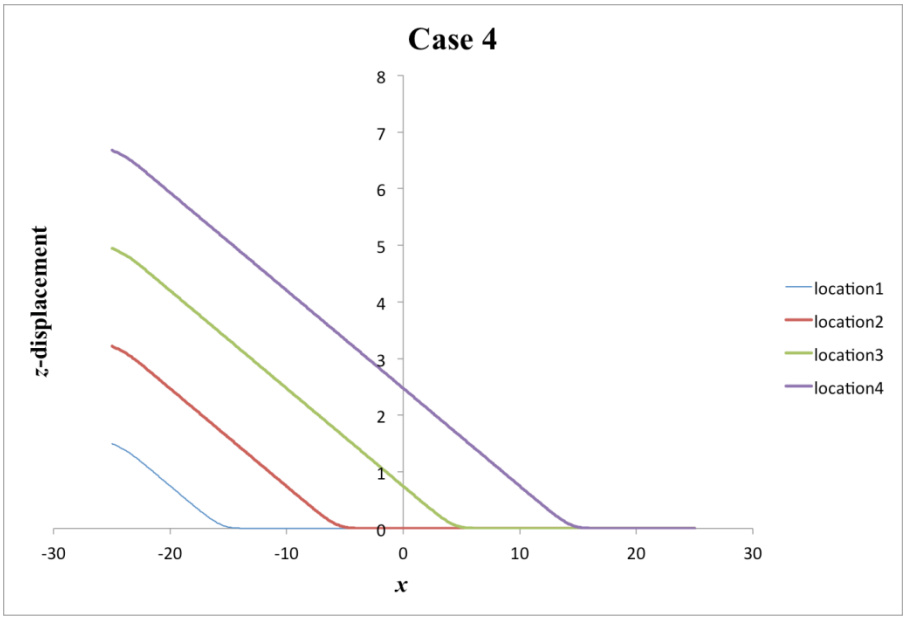

Figure 18: *Z*-displacement plot for Case 4 at the 4 front locations.

The results in Table 1 for x_f / u_z are 5.99, 17.7, 1.82 and 5.99 for each of the 4 Cases suggests a similar relationship as the area strain to the parameters, which can also be shown from Figures 15-18. The cell surface takes on a linear shape due to the fact that the cells move at a constant rate in the normal direction and the commencement front propagates at a constant speed in the *x*-direction. A larger value of c_0 / v_0 makes the commencement front move faster in the in-plane direction.

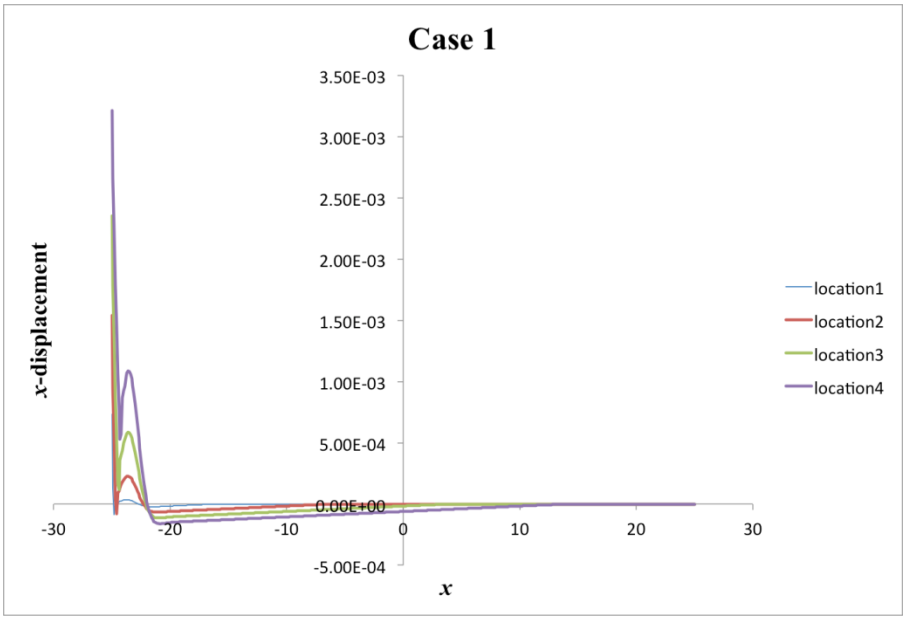

Figure 19: *X*-displacement plot for Case 1 at the 4 front locations.

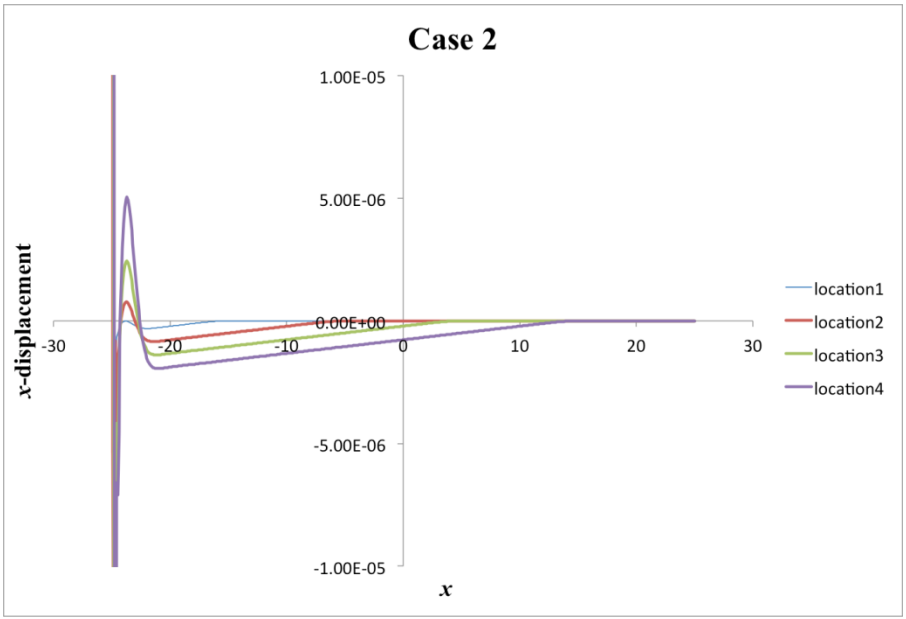

Figure 20: *X*-displacement plot for Case 2 at the 4 front locations.

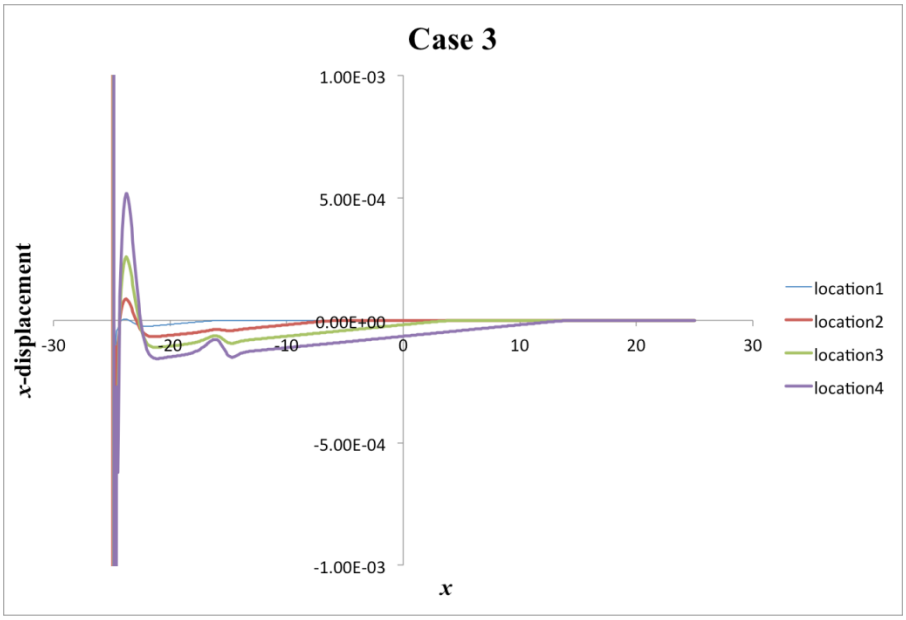

Figure 21: *X*-displacement plot for Case 3 at the 4 front locations.

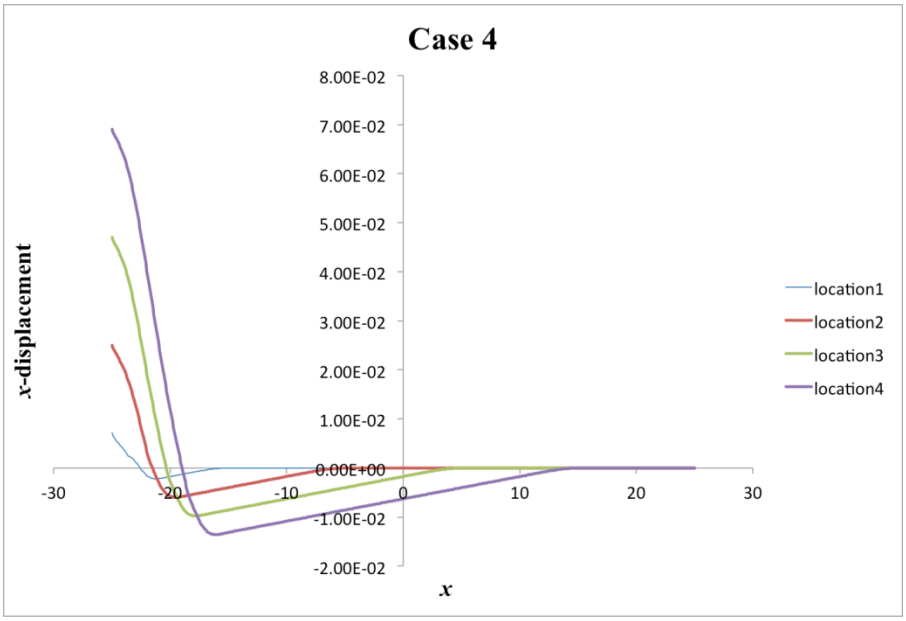

Figure 22: *X*-displacement plot for Case 4 at the 4 front locations.

Figures 19-22 are the in-plane displacement profiles for the cell sheet, showing some features of wave-like behavior mentioned above such that the *x*-displacement

reaches a peak value on the left edge and falls with location moving to the right, and then reaches a negative peak value and then returns to zero. The magnitude of this "wave" $u_x^{\max}$ grows through time. We can see that the approximate magnitude for each Case at the 4th commencement front location is 1e-3, 5e-6, 5e-4 and 1e-2 respectively. The crest moves to the right a as time goes by. Each of the parameters have effect on $u_x^{\max}$. Larger values of c_0 will make the magnitude smaller as proven in Cases 1 and 2. Raising v_0 will also decrease $u_x^{\max}$ as seen in the comparison between Cases 1 and 3. Lastly, κ has a positive relationship with $u_x^{\max}$ as shown in Cases 1 and 4, with increasing κ causing larger values of $u_x^{\max}$.

5.4 Surface with One Curvature

Finally, we present simulations on a surface with one curvature. For these simulations on the curved-surface, we set $c_0 = 6$, $v_0 = 0.01$ and $\kappa = 0.015$ in an attempt to mimic observed growth patterns. The function for the one-radius-of-curvature surface (see Figure 23 below) is defined as

$$z = a_2\left(1 - y^2\right) \tag{5.10}$$

This surface has one curvature, i.e. the normal vector in *x*-direction is always 0. The parameter a_2 is a constant to determine the curvature. We set $a_2 = 0.05$ in this simulation.

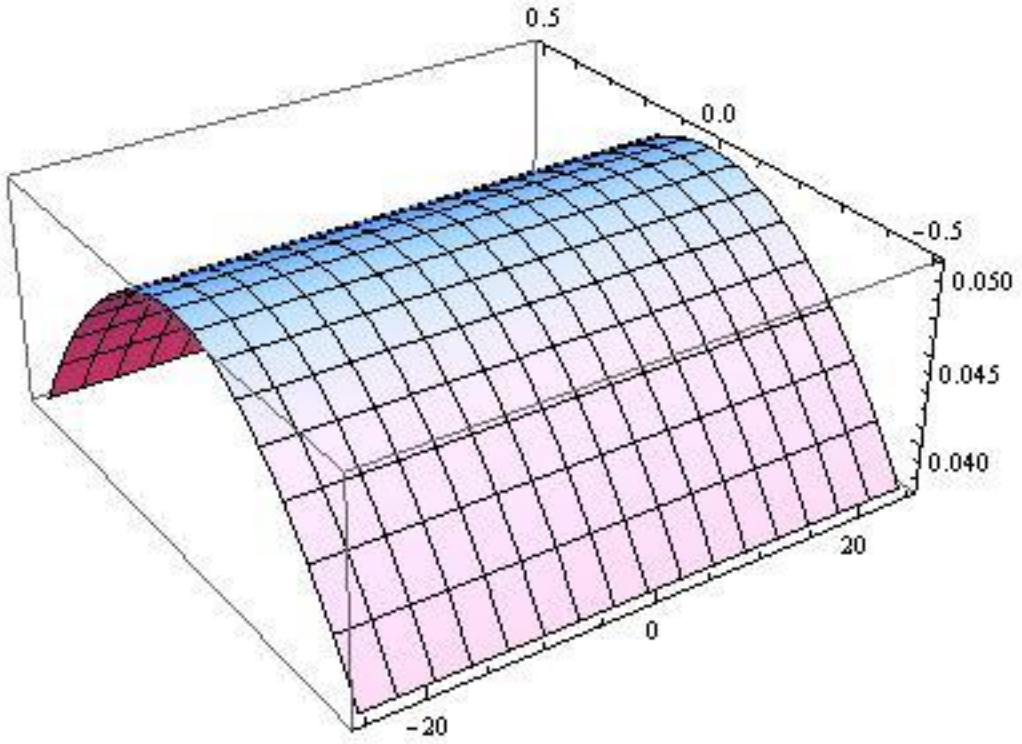

Figure 23: The surface with one radius of curvature.

Below we show the results for the model on this curved surface over time. Similar to the flat surface, we will evaluate the phase-field distribution to track the commencement front, the strain distribution as cell motions are driven by that in the theory, the normal displacement to study its out-of-plane behavior and the x-displacement for the in-plane phenomenon.

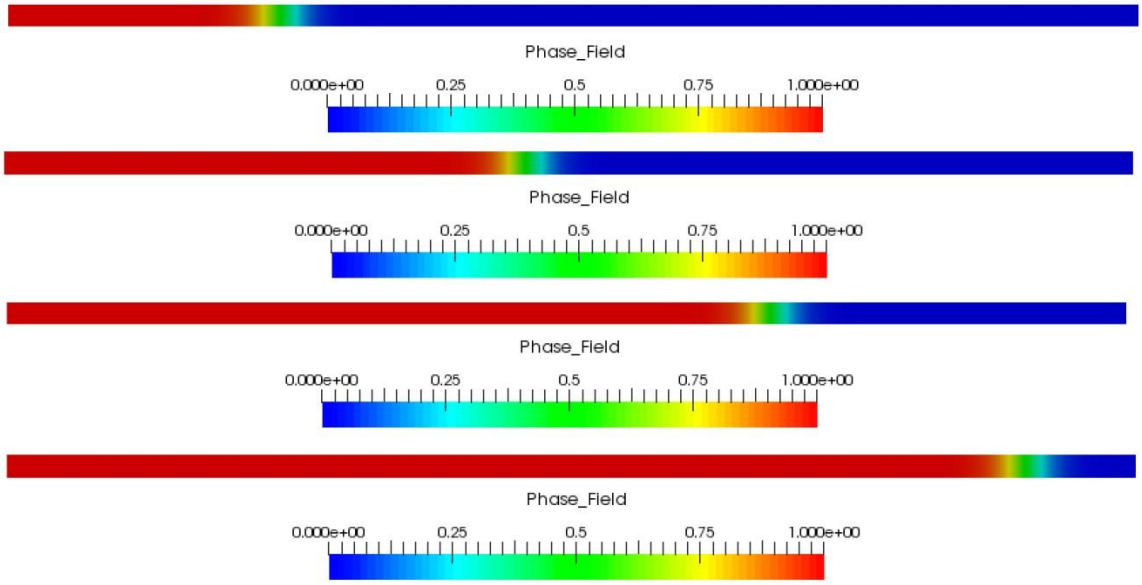

Figure 24: Phase-field plot indicating the location of the commencement front at 4 commencement front locations for a surface with one curvature.

Again, in Figure 24 we will see that the commencement front moves and transits smoothly; for secretory cells $\phi = 1$ while non-secretory cells have $\phi = 0$. Different from the flat surface, cells on the same *x* location may not have the same value of the order parameter; instead, cells on the edge are retarded and form a C-shape because of the curvature, although this effect is subtle for small curvatures.

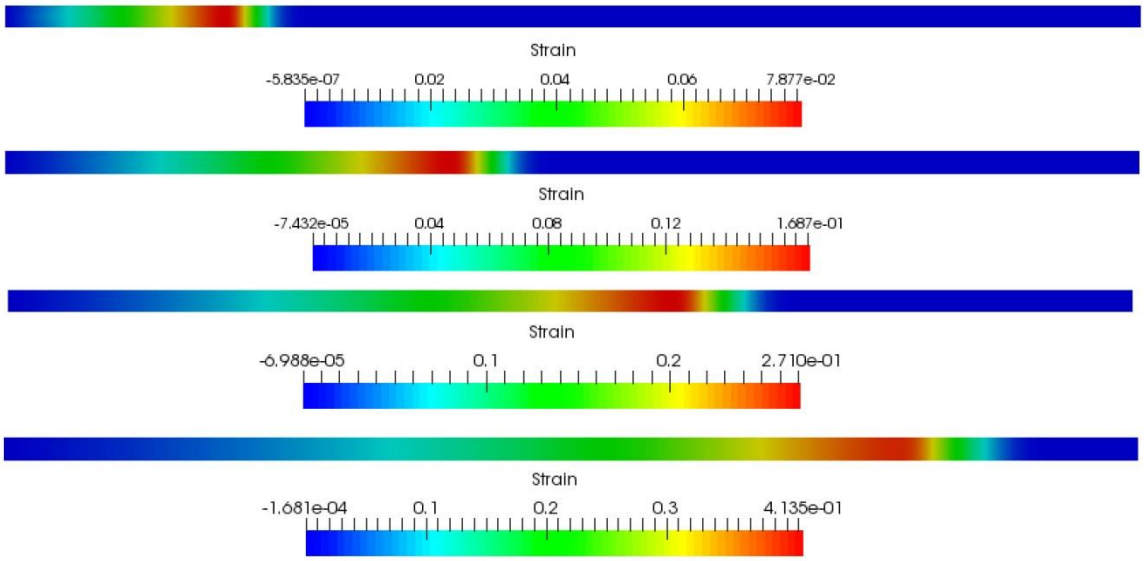

Figure 25: Strain plot at 4 commencement front locations for a surface with one curvature.

Unlike the flat surface, the strain of the curved surface does not reach a peak value but keeps increasing through time from 0 to 42% as shown in Figure 25, which is much higher than what we obtained for the flat surface.

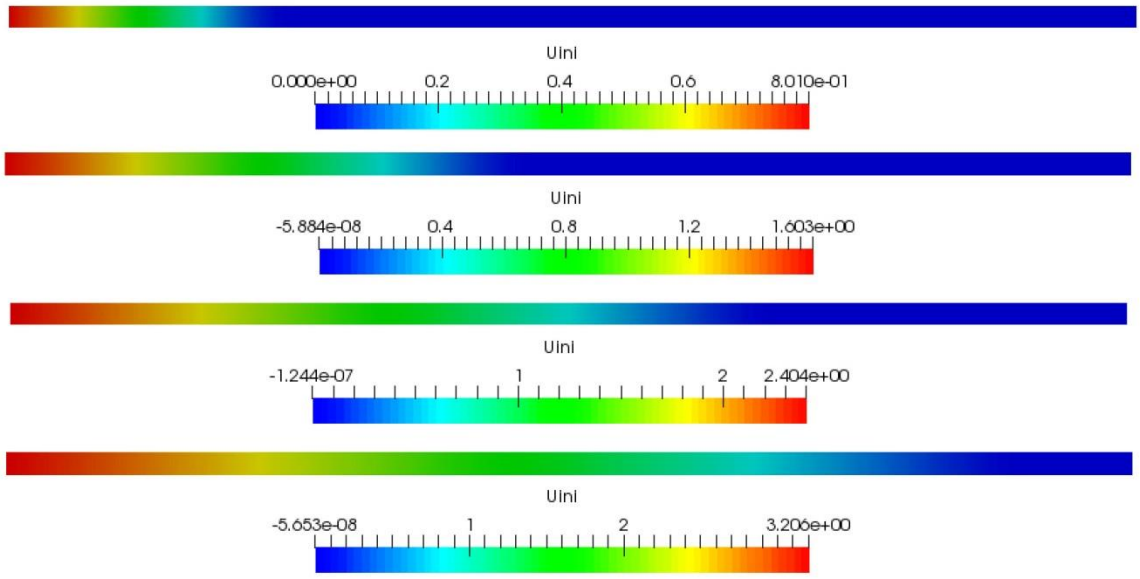

Figure 26: Normal-displacement plot at 4 commencement front locations for a surface with one curvature.

Figure 26 shows the normal motion of the curved surface. It follows a similar pattern for the flat surface that is being lifted up at a constant velocity as the commencement front moves forward. However, it seems that x_f / u_z is much higher than that of the flat surface. Possibly this is due to the larger strains that cause in-plane rearrangements to be faster.

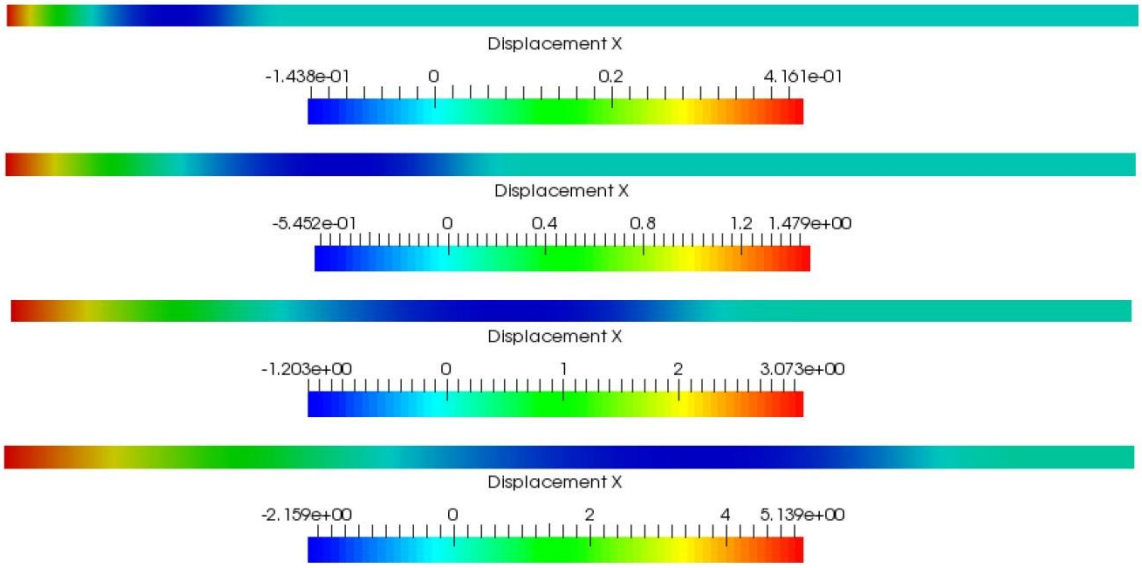

Figure 27: *X*-displacement plot at 4 commencement front locations for a surface with one curvature.

Wave-like behavior still exists for the curved surface as Figure 27 shows. The color red represents a positive displacement while the color blue represents a negative one. Again, the *x*-displacement reaches a peak value on the left edge and falls down with location moving to the right, and then reaches a negative peak value and returns to zero. Compared to the flat surface, magnitude of this "wave" is much bigger, nearly 5.14 before the commencement front reaches the end of the sheet. Also, this is possibly due to the large strain that causes in-plane rearrangements to be more intense.

5.5 DEJ

The dental enamel can be considered a doubly-curved surface when matching to images for wild-type mice. An approximation for the DEJ surface can be specified by the analytical representation,

$$z = z_0 - (b+y)\left[\sqrt{a_2 + y^2} - a_2\right] + \rho - \sqrt{\rho^2 + x^2} \tag{5.11}$$

with $a_2 > 0$, $b > 0$, $\rho > 0$, and z_0 a constant. It is illustrated in Figure 26. The function z has uniform radius of curvature ρ along the axis of the tooth (x-axis, length direction). On sections transverse to the axis of the tooth (width direction), it exhibits a peak at $y = 0$ where the radius of curvature takes the maximum value $\rho_y = a_2 / b$. z is approximately a skewed parabola, with the skewness controlled by the factor $b + y$.

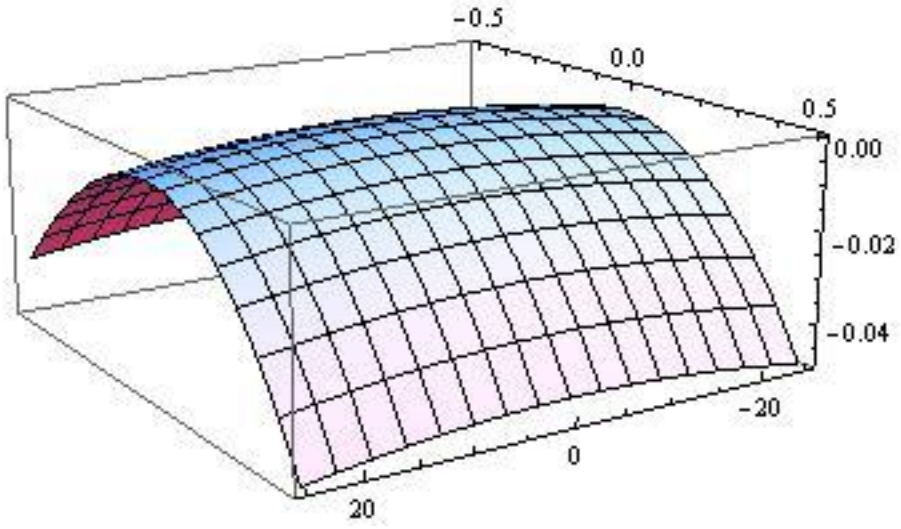

Figure 28: The doubly-curved Dental Enamel Junction.

In this work, we have not yet been able to get the commencement front move all the way through the cell sheet likely due to numerical issues associated with the mesh density and time integration steps.

Chapter 6: Concluding Remarks and Future Work

According to basic assumptions on the migration of cells from the dental enamel junction, which are that in the normal direction to the DEJ the enamel is deposited at a constant speed, the commencement of cell growth is triggered by local strain cues, and in-plane rearrangement of the cells occurs due to strain changes and contacting neighbors, simulations on flat and curved cell sheets have been conducted in this report to simulate the deposition of enamel. Results illustrate the propagation of the commencement front and the "wave-like" in-plane displacement phenomenon. When the surface is curved, this rearrangement is more intense than for a flat surface, which causes larger strains and "wave" magnitudes. The parameters c_0, v_0 and κ play a significant role in the velocity of the commencement front and the magnitude of the strains. Also, boundary conditions on the edges which restrict nodes there from moving in the direction out of the sheet are important; otherwise non-physical behaviors can occur. Future work will involve adjusting the parameters and curvatures to make the commencement front move through a doubly-curved surface such as DEJ as well as to get the results in closer agreement with experimental observations. Furthermore, studying not only the motion of the three dimensional surface, but also the in-plane pattern formation to understand how the dental enamel gets its stripes will be of interest.

References

1. Boyde, A., 1989. Enamel. In: Oksche, A., Vollrath, L. (Eds.), Handbook of Microscopic Anatomy. Springer, Berlin, pp. 309–473.

2. Boyde, A., Fortelius, M., Lester, K.S., Martin, L.B., 1988. Basis of the structure and development of mammalian enamel as seen by scanning electron-microscopy. Scanning Microscopy 2 (3), 1479–1490

3. Gartner, L.P., Hiatt, J.L., 2005. Color Atlas of Histology. Lippincott, Williams & Wilkins, Philadelphia.

4. Nanci, A. (Ed.), 2003. Ten Cate's Oral Histology: Development, Structure, and Function. Mosby, St. Louis, Missouri (copyright Elsevier).

5. White, S.N., Luo, W., Paine, M.L., Fong, H., Sarikaya, M., Snead, M.L., 2001. Biological organization of hydroxyapatite crystallites into a fibrous continuum toughens and controls anisotropy in human enamel. Journal of Dental Research 80 (1), 321–326.

6. Cox BN. 2010 A multi-scale, discrete-cell simulation of organogenesis: application to the effects of strain stimulus on collective cell behavior during ameloblast migration. J. Theor. Biol. 262, 58–72.(doi:10.1016/j.jtbi.2009.09.010)

7. Turing AM. 1952 The chemical basis of morphogenesis. Phil. Trans. R. Soc. Lond. B 237, 37–72. (doi:10.1098/rstb.1952.0012)

8. Harrison LG. 1993 Kinetic theory of living pattern. Cambridge, UK: Cambridge University Press.

9. Folkman J, Moscona A. 1978 Role of cell shape in growth control. Nature 273, 345–349. (doi:10.1038/273345a0)

10. Rot-Nikcevic I, Reddy T, Downing KJ, Belliveau AC, Hallgrimson B, Hall BK, Kahlar B. 2006 Myf5-/-: MyoD-/- amyogenic fetuses reveal the importance of early contraction and static loading by striated muscle in mouse skeletogenesis. Dev. Genes Evol. 216, 1–9. (doi:10.1007/s00427-005-0024-9)

11. Nelson CM, Jean RP, Tan JL, Liu WF, Sniadecki NJ, Spector AA, Chen CS. 2005 Emergent patterns of growth controlled by multicellular form and mechanics. Proc. Natl Acad. Sci. USA 102, 11 594–11599. (doi:10.1073/pnas.0502575102)

12. Hamant O et al. 2008 Developmental patterning by mechanical signals in Arabidopsis. Science 322, 1650–1655. (doi:10.1126/science.1165594)

13. Keller R, Davidson LA, Shook DR. 2003 How we are shaped: the biomechanics of gastrulation. Differentiation 71, 171–205. (doi:10.1046/j.1432-0436.2003.710301.x)

14. Kolega J. 1986 Effects of mechanical tension on protrusive activity and microfilament and intermediate filament organization in an epidermal epithelium moving in culture. J. Cell Biol. 102, 1400–1411. (doi:10.1083/jcb.102.4.1400)

15. Li B, Li F, Puskar KM, Wang JH-C. 2009 Spatial patterning of cell proliferation and differentiation depends on mechanical stress magnitude. J. Biomech. 42, 1622–1627. (doi:10.1016/j.jbiomech.2009.04.033)

16. Lo C-M, Wang H-B, Dembo M, Wang Y-L. 2000 Cell movement is guided by the rigidity of the substrate. Biophys. J. 79, 144–152. (doi:10.1016/S0006-3495(00)76279-5)

17. Pelham Jr RJ, Wang Y. 1997 Cell locomotion and focal adhesions are regulated by substrate flexibility. Proc. Natl Acad. Sci. USA 94, 13 661–13 665. (doi:10.1073/pnas.94.25.13661)

18. Cox B N. 2013 How the tooth got its stripes: patterning via strain-cued motility[J]. J. R. Soc. Interface, 10, 20130266.

19. Garikapti, K., Arruda, E.M., Grosh, K., Narayanan, H., 2004. A continuum treatment of growth in biological tissue: the coupling of mass transport and mechanics. Journal of the Mechanics and Physics of Solids 52, 1595–1625.

20. Kuhl, E., Menzel, A., Steinmann, P., 2003. Computational modeling of growth: a critical review, a classification of concepts and two new consistent approaches. Computational Mechanics 32, 71–88.

21. Kuhl, E., Maas, R., Himpel, G., Menzel, A., 2007. Computational modeling of arterial wall growth. Biomechanical Modeling and Mechanobiology 6, 321–331.

22. Rodriguez, E.K., Hoger, A., McCulloch, A.D., 1994. Stress-dependent finite growth in soft elastic tissues. Journal of Biomechanics 27, 455–467.

23. Fried E, Gurtin M E. 1993 Continuum theory of thermally induced phase transitions based on an order parameter. Physica D: Nonlinear Phenomena 68, 326-343.

24. Fried E, Gurtin M E. 1994 Dynamic solid-solid transitions with phase characterized by an order parameter. Physica D: Nonlinear Phenomena 72, 287-308.

25. Gurtin M E. 1996 Generalized Ginzburg-Landau and Cahn-Hilliard equations based on a microforce balance. Physica D: Nonlinear Phenomena 92, 178-192.

26. Chen X, Yin J. 2010 Buckling patterns of thin films on curved compliant substrates with applications to morphogenesis and three-dimensional microfabrication. Soft Matter 6, 5667–5680. (doi:10.1039/c0sm00401d)